Proper Orthogonal Decomposition-Based Modeling, Analysis, and Simulation of Dynamic Wind Load Effects on Structures

Xinzhong Chen[1] and Ahsan Kareem[2]

Abstract: Multicorrelated stationary random processes/fields can be decomposed into a set of subprocesses by diagonalizing their covariance or cross power spectral density (XPSD) matrices through the eigenvector/modal decomposition. This proper orthogonal decomposition (POD) technique offers physically meaningful insight into the process as each eigenmode may be characterized on the basis of its spatial distribution. It also facilitates characterization and compression of a large number of multicorrelated random processes by ignoring some of the higher eigenmodes associated with smaller eigenvalues. In this paper, the theoretical background of the POD technique based on the decomposition of the covariance and XPSD matrices is presented. A physically meaningful linkage between the wind loads and the attendant background and resonant response of structures in the POD framework is established. This helps in better understanding how structures respond to the spatiotemporally varying dynamic loads. Utilizing the POD-based modal representation, schemes for simulation and state-space modeling of random fields are presented. Finally, the accuracy and effectiveness of the reduced-order modeling in representing local and global wind loads and their effects on a wind-excited building are investigated.

Introduction

Multicorrelated stationary random processes/fields, such as wind velocity and pressure fluctuations, on structures can be transformed into a set of subprocesses by diagonalizing their covariance or cross power spectral density (XPSD) matrices through either the Cholesky (lower or upper triangular) or Schur (eigenvector) decomposition. The eigenvector decomposition offers physically meaningful insight into the process as each eigenvector (eigenmode) may be characterized on the basis of its spatial distribution. It is also recognized that only a small number of eigenmodes corresponding to eigenvalues with larger magnitudes are dominant, such that one may ignore some of the eigenmodes associated with small eigenvalues in the description of a large-size random field. Accordingly, this technique provides a unique tool for data compression and facilitates a reduced-order modeling of large-size random fields. The eigenvector decomposition is theoretically based on the Karhunen–Loeve expansion, which is also known as the proper orthogonal decomposition (POD) (e.g., Loeve 1963).

The POD technique based on the covariance matrix has been widely used in many fields, such as fluid mechanics, image processing, signal analysis, data compression, and others. Lumley (1970) and Armitt (1968) introduced this technique to address turbulence and wind-related problems, respectively, and it was later used by many researchers in describing pressure fluctuations on buildings and structures and a host of wind-related problems (e.g., Lee 1975; Kareem 1978; Kareem and Cermak 1984; Holmes 1992; Davenport 1995; Kareem 1999; Tamura et al. 1999; Carassale et al. 2000). In stochastic structural mechanics, the POD technique based on the covariance matrix has been utilized for the simulation of spatially varying correlated random variables (e.g., Yamazaki and Shinozuka 1990), stochastic finite element analysis (e.g., Ghanem and Spanos 1991), and stochastic dynamics (Vasta and Schueller 2000).

The Cholesky decomposition of XPSD matrix has been widely utilized in digital simulation of a vector-valued stationary random process (Shinozuka and Jan 1972). Li and Kareem (1989, 1993) introduced the concept of stochastic decomposition of the XPSD matrix for the simulation of stationary random processes, which was further extended to the simulation of nonstationary processes (Li and Kareem 1991, 1997). Central to the stochastic decomposition is the decomposition of a correlated vector-valued random process into a set of vector-valued subprocesses, such that any two component processes from the same subprocess are statistically fully coherent, while any two component processes from different subprocesses are noncoherent. Therefore, simulation of the parent process is simplified by the simulation of noncoherent subprocesses. The Schur decomposition is often more attractive than the Cholesky decomposition as the former permits a relatively small number of modes to be utilized in the simulation of random fields (Shinozuku et al. 1990; Di Paola and Gullo 2001). Examples of stochastic decomposition in the dynamic response analysis of structures under wind, waves, and seismic excitations

[1]Assistant Professor, Wind Science and Engineering Research Center, Dept. of Civil Engineering, Texas Tech Univ., Lubbock, TX 79409.

[2]Robert M. Moran Professor, Dept. of Civil Engineering and Geological Sciences, Univ. of Notre Dame, Notre Dame, IN 46556. E-mail: kareem@nd.edu

can be found, for example, Li and Kareem (1993, 1995), Lin et al. (1994), Xu et al. (1999), and Carassale et al. (2001).

Response analysis and design of structural control involving a feed-forward link with the modern system theory requires a state-space model of the loading, which is augmented to the structural state-space model for integrated state-space modeling of the overall system. The state-space modeling of multicorrelated wind fluctuations was addressed in Goßmann and Walter (1983), Suhardjo et al. (1992), Matsumoto et al. (1996), and Kareem (1997). These applications were based on the factorization of the XPSD matrix and subsequent realization of the transfer function matrix. These operations were noted to be nontrivial for a large-size random field which rendered the state-space modeling a challenging task. To address these issues, in Kareem (1999), Benfratello and Muscolino (1999), and Kareem and Mei (2000), frameworks using the XPSD matrix-based POD were presented with an approximation of the frequency dependent eigenvectors represented by constant values at a fixed frequency. Chen and Kareem (2001) presented a framework based on a multivariate autoregressive (AR) model.

The numerical advantage of the POD technique, akin to the modal analysis in structural dynamics, relies on the reduced-order representation through truncation of the higher eigenmodes associated with small eigenvalues. This reduced-order representation, of course, must warrant that the important characteristics of the random field and related quantities remain unchanged, or the modification resulting from the approximate representation is acceptable. Several studies on the covariance matrix-based POD technique have demonstrated that truncating higher wind loading modes helps to expedite computations of global wind loads and their effects (e.g., Bienkiewicz et al. 1995; Holmes et al. 1997; Tamura et al. 1999; Chen and Kareem 2000). However, truncation of higher modes may not work effectively in the case of local response, which may lead to an underestimation of the local wind loads and their effects (Rocha et al. 2000). Similar observation has been made regarding the XPSD matrix-based POD technique (Chen and Kareem 2000).

In this paper, the theoretical framework of the reduced-order modeling of random vector-valued processes, using the POD technique based on both the covariance and XPSD matrices, is presented. A physically meaningful linkage between wind loads and the attendant background and resonant response of structures in the POD framework is established. Utilizing the POD modal representation, schemes for simulation and state-space modeling of random fields are presented. Finally, the accuracy and effectiveness of the reduced-order modeling in representing local and global wind loads and their effects on a wind-excited building are investigated.

Covariance Matrix-Based Proper Orthogonal Decomposition

Let $\mathbf{P}(t) = \{P_1(t), P_2(t), \ldots, P_N(t)\}^T$ be a discrete zero-mean vector-valued stationary random process, which can be expanded in terms of a set of normalized orthogonal mode functions $\mathbf{\Phi}$ as

$$\mathbf{P}(t) = \mathbf{\Phi}\mathbf{a}(t) = \sum_{n=1}^{N} \mathbf{\Phi}_n a_n(t) = \sum_{n=1}^{N} \bar{\mathbf{P}}_n(t) \tag{1}$$

where $\mathbf{\Phi} = [\mathbf{\Phi}_1, \mathbf{\Phi}_2, \ldots, \mathbf{\Phi}_N]$; $\mathbf{\Phi}^T\mathbf{\Phi} = \mathbf{I}$; $\mathbf{a}(t) = \mathbf{\Phi}^T\mathbf{P}(t) =$ expansion series; $\bar{\mathbf{P}}_n(t) = \mathbf{\Phi}_n a_n(t) = n$th subprocess; $\mathbf{I} =$ unity matrix; and superscript T denotes the matrix transpose operator.

It can be demonstrated that the mode functions, $\mathbf{\Phi}_n$ ($n = 1, 2, \ldots, N$), which optimize the projections of $\mathbf{P}(t)$, $E[|\mathbf{P}^T\mathbf{\Phi}_n|^2]$, subject to the constraint $\mathbf{\Phi}_n^T\mathbf{\Phi}_n = 1$, are defined as the solution to the following eigenvalue problem:

$$\mathbf{R}_\mathbf{P}\mathbf{\Phi}_n = \Omega_n\mathbf{\Phi}_n \tag{2}$$

where $\mathbf{R}_\mathbf{P} = E[\mathbf{P}\mathbf{P}^T] =$ covariance matrix of $\mathbf{P}(t)$; and $E[\ ] =$ mathematical expectation. Since the covariance matrix is positive definite, the eigenvalues are all real and positive, and the eigenvectors are all real.

The covariance matrix of $\mathbf{a}(t)$ and that between $\bar{\mathbf{P}}_n(t)$ and $\bar{\mathbf{P}}_m(t)$ ($n, m = 1, 2, \ldots, N$) are given by

$$\mathbf{R}_\mathbf{a} = \mathbf{\Phi}^T\mathbf{R}_\mathbf{P}\mathbf{\Phi} = \mathbf{\Omega} = \text{diag}[\Omega_1, \Omega_2, \ldots, \Omega_N] \tag{3}$$

$$\mathbf{R}_{\bar{\mathbf{P}}_n\bar{\mathbf{P}}_m} = \Omega_n\mathbf{\Phi}_n\mathbf{\Phi}_m^T\delta_{nm} \tag{4}$$

where $\delta_{mn} =$ Kronecker delta. Thus, the POD representation decomposes the correlated vector-valued process into a set of subprocesses which are uncorrelated at zero-time lag. Using this attribute, the covariance matrix $\mathbf{R}_\mathbf{P}$ is consequently expressed in terms of mode functions as

$$\mathbf{R}_\mathbf{P} = \mathbf{\Phi}\mathbf{\Omega}\mathbf{\Phi}^T = \sum_{n=1}^{N} \Omega_n\mathbf{\Phi}_n\mathbf{\Phi}_n^T \tag{5}$$

which obviously captures the contribution of each mode to the covariance. Furthermore, the following relationship

$$E[\mathbf{P}^T\mathbf{P}] = E[\mathbf{a}^T\mathbf{a}] = \sum_{n=1}^{N} \Omega_n \tag{6}$$

indicates that the sum of the mean square values of the original process remains unchanged in the POD representation, and it is equal to the sum of the eigenvalues of the covariance matrix.

It is also worth pointing at that the POD representation is the most efficient representation of the random process in terms of truncated expansion series. By ordering the eigenvalues in a decreasing order, the reduced-order representation in terms of first N_R ($N_R < N$) orthogonal mode functions given by

$$\hat{\mathbf{P}}(t) = \sum_{n=1}^{N_R} \mathbf{\Phi}_n a_n(t) = \sum_{n=1}^{N_R} \bar{\mathbf{P}}_n(t) \tag{7}$$

= optimal representation of $\mathbf{P}(t)$ when compared to representations based on other orthogonal mode functions, which leads to a minimum error in the sum of the mean square values of the process (Therrien 1992):

$$\epsilon = E[(\mathbf{P} - \hat{\mathbf{P}})^T(\mathbf{P} - \hat{\mathbf{P}})] = \sum_{n=N_R+1}^{N} \Omega_n \tag{8}$$

In most situations, only a small number of eigenmodes associated with large eigenvalues are dominant. This attribute helps to realize a reduced-order modeling of a process through the POD representation in which higher eigenmodes associated with small eigenvalues may be truncated.

Cross Power Spectral Density Matrix-Based Proper Orthogonal Decomposition

Like the POD based on the covariance matrix, a vector-valued random process can also be decomposed based on its XPSD

matrix. The Fourier transform of the process $\mathbf{P}(t)$, $\mathbf{P}(\omega)$, can be decomposed in terms of orthogonal mode function $\mathbf{\Psi}(\omega)$ as

$$\mathbf{P}(\omega) = \mathbf{\Psi}(\omega)\mathbf{b}(\omega) = \sum_{n=1}^{N} \mathbf{\Psi}(\omega)b_n(\omega) = \sum_{n=1}^{N} \mathbf{P}_n(\omega) \qquad (9)$$

where $\mathbf{\Psi}(\omega)=[\mathbf{\Psi}_1(\omega), \mathbf{\Psi}_2(\omega), \ldots, \mathbf{\Psi}_N(\omega)]$; $\mathbf{\Psi}^*(\omega)\mathbf{\Psi}(\omega)=\mathbf{I}$; $\mathbf{b}(\omega)=\mathbf{\Psi}^*(\omega)\mathbf{P}(\omega)=$ Fourier transform of the expansion series $\mathbf{b}(t)$; $\mathbf{P}_n(\omega)=\mathbf{\Psi}_n(\omega)b_n(\omega)=$ Fourier transform of the nth subprocess $\mathbf{P}_n(t)$; and the asterisk denotes the complex conjugate and transpose operator.

The mode functions, $\mathbf{\Psi}_n(\omega)$ $(n=1,2,\ldots,N)$, that optimize the projections of $\mathbf{P}(\omega)$, $E[|\mathbf{P}^*(\omega)\mathbf{\Psi}_n(\omega)|^2]$, subject to the constraint $\mathbf{\Psi}_n^*(\omega)\mathbf{\Psi}_n(\omega)=1$, are defined as the solution to the following eigenvalue problem

$$\mathbf{S_P}(\omega)\mathbf{\Psi}_n(\omega) = \Lambda_n(\omega)\mathbf{\Psi}_n(\omega) \qquad (10)$$

where $\mathbf{S_P}(\omega)=$ double-sided XPSD matrix of $\mathbf{P}(t)$. Since the XPSD matrix is a Hermitian matrix, the eigenvalues are all real and positive, but the eigenvectors are generally complex.

The XPSD matrices of expansion series $\mathbf{b}(t)$ and the subprocesses $\mathbf{P}_n(t)$ and $\mathbf{P}_m(t)$ are given by

$$\mathbf{S_b}(\omega) = \mathbf{\Psi}^*(\omega)\mathbf{S_P}(\omega)\mathbf{\Psi}(\omega) = \mathbf{\Lambda}(\omega)$$
$$= \mathrm{diag}[\Lambda_1(\omega)\ \Lambda_2(\omega)\ \ldots\ \Lambda_N(\omega)] \qquad (11)$$

$$\mathbf{S}_{\mathbf{P}_n\mathbf{P}_m}(\omega) = \Lambda_n(\omega)\mathbf{\Psi}_n(\omega)\mathbf{\Psi}_m^*(\omega)\delta_{nm} \qquad (12)$$

Eq. (12) indicates that any two element processes from the same subprocess $\mathbf{P}_n(t)$, i.e., $P_{jn}(t)$ and $P_{kn}(t)$ $(j\neq k)$, are statistically fully coherent, while any two element processes from different subprocesses $\mathbf{P}_m(t)$ and $\mathbf{P}_n(t)$ $(m\neq n)$, i.e., $P_{jm}(t)$ and $P_{kn}(t)$, are noncoherent (Li and Kareem 1995).

Accordingly, the XPSD matrix of $\mathbf{P}(t)$ is expressed in terms of mode functions as

$$\mathbf{S_P}(\omega) = \mathbf{\Psi}(\omega)\mathbf{\Lambda}(\omega)\mathbf{\Psi}^*(\omega) = \sum_{n=1}^{N} \Lambda_n(\omega)\mathbf{\Psi}_n(\omega)\mathbf{\Psi}_n^*(\omega) \qquad (13)$$

that obviously captures the contribution of each mode to the XPSD matrix.

Similar to the covariance matrix-based POD, the reduced-order representation of the process in terms of the first N_s $(N_s < N)$ modes of the XPSD matrix associated with large eigenvalues given by

$$\hat{\mathbf{P}}(t) = \sum_{n=1}^{N_S} \mathbf{P}_n(t) \qquad (14)$$

=optimal representation of $\mathbf{P}(t)$ when compared to representations based on other orthogonal functions, which results in a minimum error in the sum of the XPSD at given frequencies, i.e., $E[\mathbf{P}^*(\omega)\mathbf{P}(\omega)]$.

It is noted that a fully coherent vector-valued process, such as ocean wave-particle kinematics with a given wave-surface profile, only has one eigenvalue and eigenmode. When the eigenmode is frequency independent, the fully coherent vector-valued process can be described by a scalar process. On the other hand, the reduced-order modeling of a noncoherent process may not be readily realized.

It should be noted that the XPSD matrix-based POD results in subprocesses that are noncoherent and thus uncorrelated at any time lag, i.e., $\mathbf{R}_{\mathbf{P}_n\mathbf{P}_m}(t)=0$ $(n\neq m)$. However, the covariance matrix-based POD results in subprocesses that are only uncorre-

lated at zero-time lag. The two POD techniques can be related by using the relationship between the covariance and XPSD matrices as

$$\mathbf{\Phi}\mathbf{\Omega}\mathbf{\Phi}^T = 2\int_0^\infty \mathbf{\Psi}(\omega)\mathbf{\Lambda}(\omega)\mathbf{\Psi}^*(\omega)d\omega \qquad (15)$$

It is noted that while the double-sided XPSD defined in the circular frequency ω domain, $\mathbf{S_P}(\omega)$, is employed in this paper, when the one-sided XPSD defined in the natural frequency $f=\omega/(2\pi)$ domain, $\mathbf{S_P}'(f)=4\pi\mathbf{S_P}(\omega)$, is utilized, the corresponding eigenvalues and eigenvectors are given by $\mathbf{\Lambda}'(f)=4\pi\mathbf{\Lambda}(\omega)$ and $\mathbf{\Phi}'(f)=\mathbf{\Phi}(\omega)$.

Proper Orthogonal Decomposition-Based Dynamic Response Analyses

Consider an N degree-of-freedom (DOF) structure described in terms of its first q modal coordinate $\mathbf{X}(t)$ under external loading $\mathbf{P}(t)$. Based on random vibration theory, the XPSD matrices of $\mathbf{X}(t)$ and relevant response $\mathbf{Y}(t)=\mathbf{GX}(t)$ are given by

$$\mathbf{S_X}(\omega) = \mathbf{H}(\omega)\mathbf{\Theta}^T\mathbf{S_P}(\omega)\mathbf{\Theta}\mathbf{H}^*(\omega) \qquad (16)$$

$$\mathbf{S_Y}(\omega) = \mathbf{G}\mathbf{S_X}(\omega)\mathbf{G}^T \qquad (17)$$

where $\mathbf{H}(\omega)=q\times q$ transfer matrix in terms of the modal coordinates; $\mathbf{\Theta}=N\times q$ structural mode shape matrix; $\mathbf{G}=\mathbf{AM\Theta}\,\mathrm{diag}[\omega_j^2]=M\times N$ participation coefficient matrix of structural modes to the response $\mathbf{Y}(t)$; $\mathbf{A}=$ the $M\times N$ influence matrix; $\mathbf{M}=$ the $N\times N$ mass matrix in physical coordinates; $\omega_j=2\pi f_j=j$th structural modal frequency.

In conventional dynamic response analysis, Eqs. (16) and (17) are directly utilized which involves a complete quadratic combination of the multimodal coupled responses. The computational effort significantly escalates with increasing modes and the number of correlated response components of interest. The computational effort could be drastically reduced by invoking the POD representation of the loading process.

Approximating $\mathbf{S_P}(\omega)$ in its first N_s $(N_s < N)$ eigenmodes, Eqs. (16) and (17) become

$$\mathbf{S_X}(\omega) \approx \sum_{n=1}^{N_s} \mathbf{E}_n(\omega)\mathbf{E}_n^*(\omega) \qquad (18)$$

$$\mathbf{S_Y}(\omega) \approx \sum_{n=1}^{N_s} \mathbf{F}_n(\omega)\mathbf{F}_n^*(\omega) \qquad (19)$$

$$\mathbf{E}_n(\omega) = \mathbf{H}(\omega)\mathbf{\Theta}^T\mathbf{\Psi}_n(\omega)\sqrt{\Lambda_n(\omega)} \qquad (20)$$

$$\mathbf{F}_n(\omega) = \mathbf{GE}_n(\omega) \qquad (21)$$

Eqs. (18)–(21) facilitate the response analysis which can be summarized in the following procedures. First, represent the external loading in terms of the POD based on the XPSD matrix with higher loading modes truncated, $\mathbf{P}_n(\omega)=\mathbf{\Psi}_n(\omega)\sqrt{\Lambda_n(\omega)}$ $(n=1,2,\ldots,N_s)$. Second, for each loading mode, calculate the corresponding responses $\mathbf{E}_n(\omega)$ and $\mathbf{F}_n(\omega)$ under the excitation $\mathbf{P}_n(\omega)$. Finally, calculate the total response by integrating the components associated with each loading mode. In this procedure, although the POD requires additional computation, the truncation of higher loading modes and the absence of coherence

among the response components associated with each loading mode drastically reduce the computational effort needed to analyze a large number of correlated structural response components.

For the seismic response of structures excited by one or a small number of ground motion components, the external loading can be expressed as $\mathbf{P}(t) = \mathbf{R}\mathbf{P}_0(t)$, where $\mathbf{R} = N \times N_0$ participation matrix; $\mathbf{P}_0(t) = N_0 \times 1$ external loading input; and N_0 = number of input ($N_0 \ll N$). The decomposition of loading $\mathbf{P}_0(t)$ significantly reduces the computational effort even without the truncation of higher loading modes.

When equations of structural motions in terms of modal coordinates are uncoupled, and the correlation among the modal response components is negligible, one has

$$\mathbf{H}(\omega) = \text{diag}[H_j(\omega)] \tag{22}$$

$$\mathbf{S_X}(\omega) = \text{diag}[S_{X_j}(\omega)] \tag{23}$$

$$H_j(\omega) = m_j[(\omega_j^2 - \omega^2) + 2i\xi_j\omega\omega_j]^{-1} \tag{24}$$

$$S_{X_j}(\omega) = |H_j(\omega)|^2 \mathbf{\Theta}_j^T \mathbf{S_P}(\omega)\mathbf{\Theta}_j \approx \sum_{n=1}^{N_S} |H_j(\omega)|^2 \chi_{jn}^2(\omega)\Lambda_n(\omega) \tag{25}$$

where m_j and ξ_j = jth generalized mass and damping ratio; and $\chi_{jn}(\omega) = \mathbf{\Theta}_j^T\mathbf{\Psi}_n(\omega)$ = projection of the jth structural mode $\mathbf{\Theta}_j$ on the jth loading mode $\mathbf{\Psi}_n(\omega)$, which offers a measure of the relative significance of the nth loading mode to the jth structural modal response; $i = \sqrt{-1}$.

In cases of lightly damped structures where the forcing function can be approximated by a white noise with a constant spectral density at the structural natural frequency, the mean square modal response can be expressed as (e.g., Kareem 1999; Carassale et al. 2001)

$$\sigma_{X_j}^2 = 2\int_0^\infty S_{X_j}(\omega)d\omega = \sum_{n=1}^{N_s} \frac{\pi\chi_{jn}^2(\omega_j)\Lambda_n(\omega_j)}{2\omega_j^3\xi_j m_j^2} \tag{26}$$

In the case where the correlation between modal response components is negligible, the square root of the sum of squares combination approach can be employed for calculating the overall response. Accordingly, the procedure involving the POD of the loading process does not necessarily provide a measurable numerical advantage. However, it may offer a clearer picture of how structures respond to spatiotemporally varying external excitations.

The wind-excited structural response is conventionally separated into a background (quasi-static) and a resonant component for computational efficiency and physical significance based on the spectral feature of wind loads and associated structural response. The background component of response $\mathbf{Y}(t)$, $\mathbf{Y}_b(t)$, can be quantified through quasi-static analysis as

$$\mathbf{Y}_b(t) = \mathbf{A}\mathbf{P}(t) \tag{27}$$

and its covariance matrix, $\mathbf{R_{Y_b}}$, is given as follows using the truncated POD of $\mathbf{R_P}$

$$\mathbf{R_{Y_b}} = \mathbf{A}\mathbf{R_P}\mathbf{A}^T \approx \sum_{n=1}^{N_R} \Omega_n \mathbf{c}_n \mathbf{c}_n^T \tag{28}$$

where $\mathbf{A} = [A_{ij}]$, A_{ij} = ith component of $\mathbf{Y}$, Y_j, under unit jth component of load $\mathbf{P}$, $P_j = 1$; $\mathbf{c}_n = \mathbf{A}\mathbf{\Phi}_n = [c_{1n}c_{2n}\ldots c_{Mn}]^T$; c_{jn} = projection

of the influence function for jth response component on the nth wind loading mode.

Eq. (28) indicates that the mean square value of the background response can be expressed in terms of the sum of components associated with each wind loading mode, which can be calculated individually. Clearly, the framework involving the covariance matrix-based POD provides a useful linkage between the wind loading mode and the background response.

The resonant component of the response is generally calculated using a modal analysis technique. Using the aforementioned procedure, the combination of the modal analysis and the POD representation of the loading offers a physically meaningful and/or computationally efficient framework.

Simulation and State-Space Modeling of Random Processes

According to the XPSD matrix-based POD technique, a multicorrelated random vector-valued process $\mathbf{P}(t)$ can be simulated by generating reduced order vector-valued subprocesses $\mathbf{P}_n(t)$ ($n = 1, 2, \ldots, N_s$). Each subprocess can be simulated individually using spectral representation, or parametric time series model or other techniques (e.g., Li and Kareem 1993; Shinozuka and Deodatis 1996; Spanos and Zeldin 1998; Mann 1998).

It is important to note that the covariance matrix-based POD technique does not lend itself as an efficient simulation tool as the decomposed subprocesses are only uncorrelated at zero time lag thus eliminating the advantage of simulating each process independently as in the case of XPSD-based POD technique. Nonetheless, this technique can be effectively utilized for the simulation of spatially varying random variables (e.g., Yamazaki and Shinozuka 1990; Ghanem and Spanos 1991), and compression and reconstruction of existing experimental data such as wind pressures on building surfaces (e.g., Tamura et al. 1999).

Spectral Representation Approach

The vector-valued subprocess $\mathbf{P}_n(t)$ with the XPSD matrix given by

$$\mathbf{S_{P_nP_n}}(\omega) = \Lambda_n(\omega)\mathbf{\Psi}_n(\omega)\mathbf{\Psi}_n^*(\omega) \tag{29}$$

can be described as

$$\mathbf{P}_n(t) = \int_{-\infty}^\infty \mathbf{\Psi}_n(\omega)\sqrt{\Lambda_n(\omega)}e^{i\omega t}dB_n(\omega) \tag{30}$$

where $B_n(\omega)$ = zero-mean Gaussian complex process with orthogonal increments, i.e.,

$$E[dB_n(\omega)] = 0; \quad dB_n(\omega) = dB_n^*(-\omega);$$

$$E[dB_n(\omega_r)dB_m^*(\omega_s)] = \delta_{\omega_r\omega_s}\delta_{nm}d\omega_r \tag{31}$$

Eq. (30) can be recast in the following discrete form for an element process as

$$P_{jn}(t) = \sum_{n_1=-N_1}^{N_1-1} \Psi_{jn}(\omega_{n_1})\sqrt{\Lambda_n(\omega_{n_1})}e^{i\omega_{n_1}t}\Delta B_{n_1}$$

$$= \sum_{n_1=0}^{N_1-1} \sqrt{2}|\Psi_{jn}(\omega_{n_1})|\sqrt{\Lambda_n(\omega_{n_1})\Delta\omega}A_{n_1n}$$

$$\times\cos(\omega_{n_1}t + \theta_{jn}(\omega_{n_1}) + \vartheta_{n_1n}) \qquad (32)$$

where $P_{jn}(t)$ $(j=1,2,\ldots,N)=j$th component of $\mathbf{P}_n(t)$; $\Psi_{jn}(\omega_{n_1})$ $=|\Psi_{jn}(\omega_{n_1})|\exp[i\theta_{jn}(\omega_{n_1})]=j$th element of $\mathbf{\Psi}_n(\omega_{n_1})$; ΔB_{n_1} $=1/\sqrt{2}\sqrt{\Delta\omega}A_{n_1n}e^{i\vartheta_{n_1n}}$; A_{n_1n} and ϑ_{n_1n}=independent random variables following a Rayleigh distribution with mean $\sqrt{\pi/2}$ and variance $(2-\pi/2)$, and uniform distribution over $[0,2\pi]$, respectively; $\Delta\omega$=frequency increment with a Nyquist (cutoff) frequency $N_1\Delta\omega$; $\omega_{n_1}=n_1\Delta\omega$; $2N_1$=total discrete number of frequencies in the interval $[-N_1\Delta\omega,N_1\Delta\omega]$.

An alternative formulation for simulation of $P_{jn}(t)$ can be expressed

$$P_{jn}(t) = \sum_{n_1=0}^{N_1-1} 2|\Psi_{jn}(\omega_{n_1})|\sqrt{\Lambda_n(\omega_{n_1})\Delta\omega}\cos(\omega_{n_1}t + \theta_{jn}(\omega_{n_1}) + \vartheta_{n_1n})$$

$$\qquad (33)$$

In the case where $\mathbf{\Psi}_n(\omega)$ can be approximated as frequency independent real-valued vector, the simulation of $\mathbf{P}_n(t)$ can be reduced to simulation of a scalar process with a power spectrum of $\Lambda_n(\omega)$.

A similar formulation employing the Cholesky decomposition can be obtained by replacing $\mathbf{\Psi}(\omega)\sqrt{\mathbf{\Lambda}(\omega)}$ with $\mathbf{L}_S(\omega)$, where $\mathbf{L}_S(\omega)$=lower/upper triangular matrix given by $\mathbf{S_P}(\omega)$ $=\mathbf{L}_S(\omega)\mathbf{L}_S^*(\omega)$, which has been widely utilized in Monte Carlo simulation (e.g., Shinozuka and Jan 1972).

For an example, a two-dimensional univariate zero-mean homogeneous continuous random field $f(x,t)$ in space $-\infty<x<\infty$ and time $-\infty<t<\infty$ is considered. The autocorrelation function $R_{xt}(\xi,\tau)=E[f(x,t)f(x+\xi,t+\tau)]$ and power spectral density (PSD) function $S_{xt}(\kappa,\omega)$ are related by

$$S_{xt}(\kappa,\omega) = \frac{1}{(2\pi)^2}\int_{-\infty}^{\infty} R_{xt}(\xi,\tau)e^{-i(\kappa\xi+\omega\tau)}d\xi d\tau \qquad (34)$$

$$R_{xt}(\xi,\tau) = \int_{-\infty}^{\infty} S_{xt}(\kappa,\omega)e^{i(\kappa\xi+\omega\tau)}d\kappa d\omega \qquad (35)$$

and the XPSD between $f(x,t)$ and $f(x+\xi,t)$ is given by

$$S_t(\xi,\omega) = \int_{-\infty}^{\infty} S_{xt}(\kappa,\omega)e^{i\kappa\xi}d\kappa \qquad (36)$$

In many practical situations, stationary random fields have PSD functions that are band limited. In these cases, it is assumed that $S_{xt}(\kappa,\omega)$ is zero outside of the region $-\kappa_u\leq\kappa\leq\kappa_u$ and $-\omega_u\leq\omega\leq\omega_u$ [where κ_u and ω_u=Nyquist (cutoff) wave number and frequency, respectively], and it is discrete within this region with $2N_2$ and $2N_1$ uniform increments $\Delta\kappa=\kappa_u/N_2$ and $\Delta\omega=\omega_u/N_1$ along κ and ω axes, respectively. The corresponding correlation and XPSD functions become

$$R_{xt}(\xi,\tau) = \sum_{n_2=-N_2}^{N_2-1}\sum_{n_1=-N_1}^{N_1-1} S_{xt}(\kappa_{n_2},\omega_{n_1})e^{i(\kappa_{n_2}\xi+\omega_{n_1}\tau)}\Delta\kappa\Delta\omega \qquad (37)$$

$$S_t(\xi,\omega) = \sum_{n_2=-N_2}^{N_2-1} S_{xt}(\kappa_{n_2},\omega)e^{i\kappa_{n_2}\xi}\Delta\kappa \qquad (38)$$

where $\kappa_{n_2}=n_2\Delta\kappa$; $\omega_{n_1}=n_1\Delta\omega$.

It is obvious that $R_{xt}(\xi,\tau)$ and $S_t(\xi,\omega)$ given by Eqs. (37) and (38) will be sufficiently accurate representations of these functions given by Eqs. (35) and (36), at the region $-L/2\leq\xi\leq L/2$ and $-T/2\leq\xi\leq T/2$ (where $L=2\pi/\Delta\kappa$, $T=2\pi/\Delta\omega$), and the region $-L/2\leq\xi\leq L/2$ and $-\omega_u\leq\omega\leq\omega_u$, respectively. However, these functions become periodic functions along the x and t axes with periods L and T for $R_{xt}(\xi,\tau)$, and along the x axis with a period L for $S_t(\xi,\omega)$. Accordingly, the random field $f(x,t)$ also becomes a periodic random field along the x and t axes with periods L and T, respectively, as $E[(f(x,t)-f(x+L,t+T))^2]$ $=[2R_{xt}(0,0)-2R_{xt}(L,T)]=0$.

Consider the POD formulation of the periodic random field $f(x,t)$ expressed by

$$\int_0^L S_t(x_2-x_1,\omega)\Phi_n(x_2,\omega)dx = \Lambda_n(\omega)\Psi_n(x_1,\omega) \qquad (39)$$

and utilizing the periodicity of $S_x(\xi,\omega)$, it can be readily illustrated that the POD basis function $\Phi_n(x,\omega)$ $(n=0,\pm1,\pm2,\ldots)$ is identical to the following Fourier basis function

$$\Psi_n(x,\omega) = \frac{1}{\sqrt{L}}e^{i\kappa_nx} \qquad (40)$$

and the associated eigenvalue becomes the PSD as

$$\Lambda_n(\omega) = \int_{-L/2}^{L/2} S_t(\xi,\omega)e^{i\kappa_n\xi}d\xi = 2\pi S_{xt}(-\kappa_n,\omega) = 2\pi S_{xt}(\kappa_n,\omega) \qquad (41)$$

A similar discussion concerning the POD of correlation function of a scalar discrete random process was presented in Therrien (1992).

Accordingly, $f(x,t)$ can be represented as follows similar to Eq. (34)

$$f(x,t) = \sum_{n_2=0}^{N_2-1}\sum_{n_1=0}^{N_1-1} 2\sqrt{S_{xt}(\kappa_{n_2},\omega_{n_1})\Delta\kappa\Delta\omega}\{\cos(\omega_{n_1}t + \kappa_{n_2}x + \vartheta_{n_1n_2}^{(1)})$$

$$+ \cos(\omega_{n_1}t - \kappa_{n_2}x + \vartheta_{n_1n_2}^{(2)})\} \qquad (42)$$

where $\vartheta_{n_1n_2}^{(1)}$ and $\vartheta_{n_1n_2}^{(2)}$=two different sets of random phase angles with uniform distributions over $[0,2\pi]$. It should be noted that the above formulation has been derived in Shinozuka and Deodatis (1996) utilizing an alternative approach.

It should be emphasized that the preceding representation of $f(x,t)$ is realized by discrete representation of band limited $S_{xt}(\kappa,\omega)$ in the region $-\kappa_u\leq\kappa\leq\kappa_u$ and $-\omega_u\leq\omega\leq\omega_u$, which corresponds to the representation of $R_{xt}(\xi,\tau)$ in the region $-L/2\leq\xi\leq L/2$ and $-T/2\leq\tau\leq T/2$. In cases where the correlation function decays with increase in separation and approaches zero when the separation becomes sufficiently large, the random field given by Eq. (42) will serve as a sufficiently accurate representation of the original random field when $\Delta\kappa$ and $\Delta\omega$ are sufficiently small, i.e., L and T are sufficiently large.

The results for the periodic random field has further implications for general random field that are not periodic or almost periodic. Consider the POD formulation of the general random field $f(x,t)$ defined by

$$\int_0^{L_0} S_t(x_2 - x_1, \omega)\Phi_n(x_2, \omega)dx = \Lambda_n(\omega)\Psi_n(x_1, \omega) \qquad (43)$$

As discussed in Therrien (1992) in the cases of scalar random processes, when L_0 is sufficiently large that the correlation function becomes approximately zero at the ends of the interval, the solution of the above POD problem will be very close to the POD for the periodic random field with a period of $2L_0$ along the x axis. Accordingly, the Fourier basis functions become a good approximation to the optimal basis functions of the POD described by Eq. (43). Therefore, for homogeneous random fields the POD does not necessarily offer advantages over the classical Fourier function decomposition. However, the POD provide an optimal representation of general inhomogeneous random fields.

For the case of continuous homogeneous wind velocity field defined in the interval $0 \leqslant x \leqslant L$ and $-\infty \leqslant t \leqslant \infty$ with double-sided XPSD function as

$$S(x_2 - x_1, \omega) = S_0(\omega)\exp\left(-\frac{c\omega|x_1 - x_2|}{2\pi U}\right) \qquad (44)$$

where c=decay factor; and U=mean wind speed, the POD formulation is defined in the following for $\Psi_n(x, \omega)$ and $\Lambda_n(\omega)$ ($n = 1, 2, \ldots$)

$$\int_0^L S(x_2 - x_1, \omega)\Phi_n(x_2, \omega)dx_2 = \Lambda_n(\omega)\Psi_n(x_1, \omega) \qquad (45)$$

which can be expressed in terms of following explicit formulations (van Trees 1968; Carassale and Solari 2002):

$$\Psi_n(x) = \frac{\alpha}{\sqrt{\mu_n^2 + \alpha^2 + 2\alpha}}\sqrt{\frac{2}{L}}\left[\sin\left(\frac{\mu_n x}{L}\right) + \frac{\mu_n}{\alpha}\cos\left(\frac{\mu_n x}{L}\right)\right] \qquad (46)$$

$$\Lambda_n(\omega) = \frac{4\alpha L S_0(\omega)}{\mu_n^2 + \alpha^2} \qquad (47)$$

where $\alpha = c\omega L/(2\pi U) = cfL/U$; and μ_n=nth root of the transcendent equation:

$$\left[\tan(\mu_n/2) + \frac{\mu_n}{\alpha}\right]\left[\tan(\mu_n/2) - \frac{\alpha}{\mu_n}\right] = 0 \qquad (48)$$

It is obvious that the eigenmodes represent sinusoidal variations. As indicated in Fig. 1(a), μ_n approaches $n\pi$ with an increase in frequency in which coherence decays faster with an increase in separation. As indicated by the value of μ_n, the eigenmodes show frequency dependent features, particularly, in the low-frequency range. As indicated in Fig. 1(b), the first eigenvalue is dominant at the lower-frequency range, whereas all eigenvalues are nearly of the same level in the higher-frequency range, indicating that all the wind modes carry the same level energy. Clearly, the computational efficiency of Monte Carlo simulation based on the POD technique can be enhanced by dropping some of the components over desired ranges of frequency without loss of accuracy.

An algorithm for generation of homogeneous wind fluctuations at uniformly distributed points along an axis in space for application to the long span bridges was proposed in Cao et al. (2000). An explicit formulation based on lower triangular matrix of the Cholesky decomposition of the XPSD matrix with given exponential coherence function was employed. In this context, it is important to point out that the POD technique offers a physi-
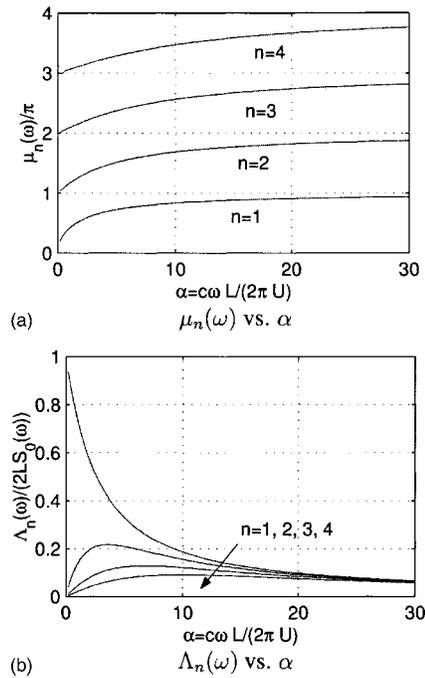

Fig. 1. Eigenvalues of a homogeneous random field

cally more meaningful and computationally more efficient scheme for simulation. It is also worth mentioning that the simulation of a homogeneous field can be directly carried out using Eq. (42), which is not constrained by the limitation that wind fluctuations must be simulated at uniformly distributed grid points, a condition necessary for the scheme introduced in Cao et al. (2000).

Parametric Time Series Modeling

Regardless of the straightforward nature of the spectral representation technique, concerns remain regarding the limitations imposed on the large number of spatially distributed simulations and the length of each time series dictated by the computer memory. Although alternative procedures to overcome this limitation are possible, these tend to compromise the attractiveness of the procedure, i.e., its inherent straightforward nature (Li and Kareem 1993; Spanos and Zeldin 1998). Utilization of parametric time series models, such as an AR model or AR moving average (ARMA) model (e.g., Li and Kareem 1990) offer other attractive venues for simulation. Herein, a framework based on the AR model is utilized for the sake of illustration. The subprocesses, $\mathbf{P}_n(t)$ ($n = 1, 2, \ldots, N_s$), are modeled as the multiple output of a system with a zero-mean unit variance Gaussian white-noise process $w_n(t)$ as an input. For each element of $\mathbf{P}_n(t)$, $P_{jn}(t)$ ($j = 1, 2, \ldots, N$), the following AR model is established individually based on its double-sided power spectrum $S_{P_{jn}}(\omega) = |\Psi_{jn}(\omega)|^2\Lambda_n(\omega)$ as

$$P_{jn}(k) = \sum_{l=1}^m a_{lj}^{(n)}P_{jn}(k - l) + \sigma_j^{(n)}w_n(k) \qquad (49)$$

where $P_{jn}(k) = P_{jn}(k\Delta t)$; Δt=time interval; m=order of the AR model; and $a_{lj}^{(n)}$ and $\sigma_j^{(n)}$=coefficients of the AR model.

The parametric time series model approach also facilitates the state-space modeling of the vector-valued random process. The
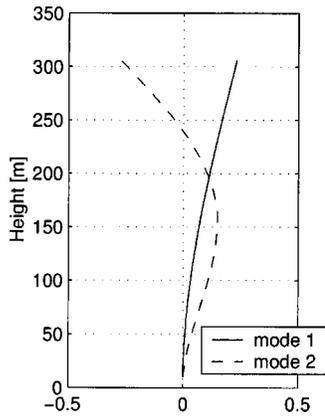
Fig. 2. Structural mode shapes

$$\mathbf{A}_j^{(n)} = \begin{bmatrix} 0 & 1 & 0 & \ldots & 0 \\ 0 & 0 & 1 & \ldots & 0 \\ \vdots & \vdots & \vdots & \ldots & \vdots \\ 0 & 0 & 0 & \ldots & 1 \\ a_{mj}^{(n)} & a_{(m-1)j}^{(n)} & a_{(m-2)j}^{(n)} & \ldots & a_{1j}^{(n)} \end{bmatrix}; \quad \mathbf{B}_j^{(n)} = \begin{bmatrix} 0 \\ 0 \\ \vdots \\ 0 \\ 1 \end{bmatrix};$$

$$\mathbf{C}_j^{(n)} = [a_{mj}^{(n)}\sigma_j^{(n)} \quad a_{(m-1)j}^{(n)}\sigma_j^{(n)} \quad \ldots \quad a_{1j}^{(n)}\sigma_j^{(n)}]; \quad D_j^{(n)} = \sigma_j^{(n)} \quad (52)$$

Accordingly, the state-space model of $\mathbf{P}_n(t)$ can be obtained by stacking these state-space models as

$$\mathbf{X}^{(n)}(k+1) = \mathbf{A}^{(n)}\mathbf{X}^{(n)}(k) + \mathbf{B}^{(n)}w_n(k) \qquad (53)$$

$$\mathbf{P}_n(k) = \mathbf{C}^{(n)}\mathbf{X}^{(n)}(k) + \mathbf{D}^{(n)}w_n(k) \qquad (54)$$

where

$$\mathbf{A}^{(n)} = \mathrm{diag}[\mathbf{A}_j^{(n)}]; \quad \mathbf{B}^{(n)} = [(\mathbf{B}_1^{(n)})^T, \ldots, (\mathbf{B}_N^{(n)})^T]^T;$$

$$\mathbf{C}^{(n)} = \mathrm{diag}[\mathbf{C}_j^{(n)}]; \quad \mathbf{D}^{(n)} = [\mathbf{D}_1^{(n)}, \ldots, \mathbf{D}_N^{(n)}]^T \qquad (55)$$

and the overall state-space model of $\mathbf{P}(t)$ is subsequently expressed as

$$\mathbf{X}(k+1) = \mathbf{AX}(k) + \mathbf{BW}(k) \qquad (56)$$

$$\mathbf{P}(k) = \mathbf{CX}(k) + \mathbf{DW}(k) \qquad (57)$$

where

$$\mathbf{A} = \mathrm{diag}[\mathbf{A}^{(n)}]; \quad \mathbf{B} = \mathrm{diag}[\mathbf{B}^{(n)}]; \quad \mathbf{C} = [\mathbf{C}^{(1)}, \ldots, \mathbf{C}^{(N_s)}];$$

following controllable canonical format of a discrete-time state-space model can be obtained for representing the AR model (Ogata 1994)

$$\mathbf{X}_j^{(n)}(k+1) = \mathbf{A}_j^{(n)}\mathbf{X}_j^{(n)}(k) + \mathbf{B}_j^{(n)}w_n(k) \qquad (50)$$

$$P_{jn}(k) = \mathbf{C}_j^{(n)}\mathbf{X}_j^{(n)}(k) + D_j^{(n)}w_n(k) \qquad (51)$$
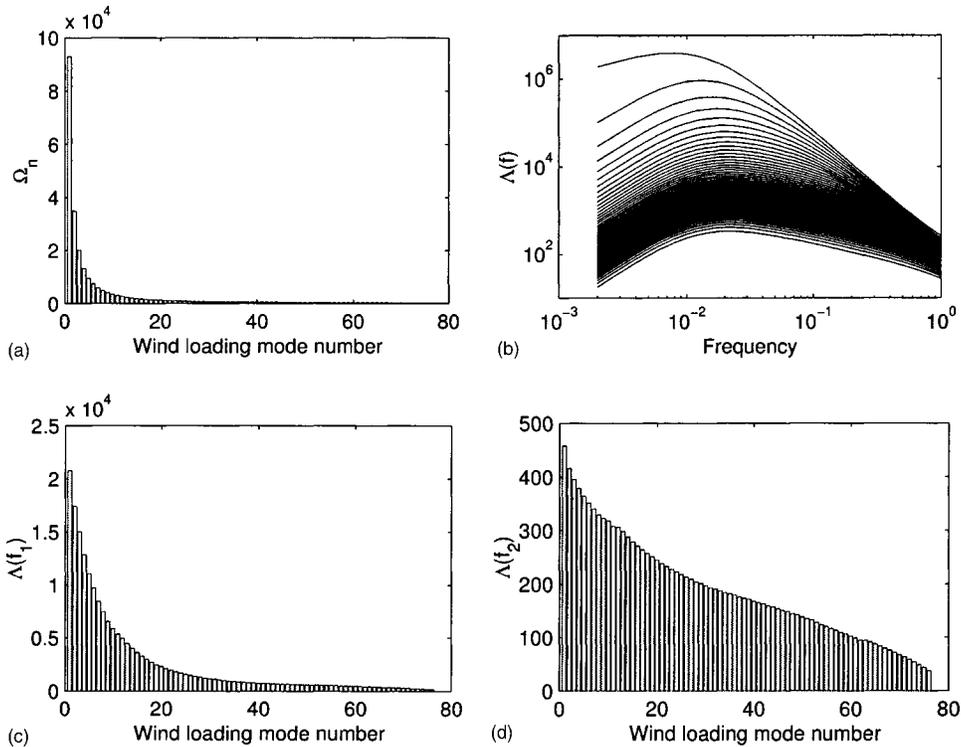
where

Fig. 3. Eigenvalues of wind loading process: (a) Based on the covariance matrix; (b) based on the cross power spectral density (XPSD) matrix (at different frequencies); (c) based on the XPSD matrix (at the first structural frequency); and (d) based on the XPSD matrix (at the second structural frequency)

Fig. 4. Wind loading mode shapes: (a) Based on the covariance matrix; (b) based on the cross power spectral density (XPSD) matrix (the first loading mode at different frequencies); (c) based on the XPSD matrix (at the first structural frequency); and (d) based on the XPSD matrix (at the second structural frequency)
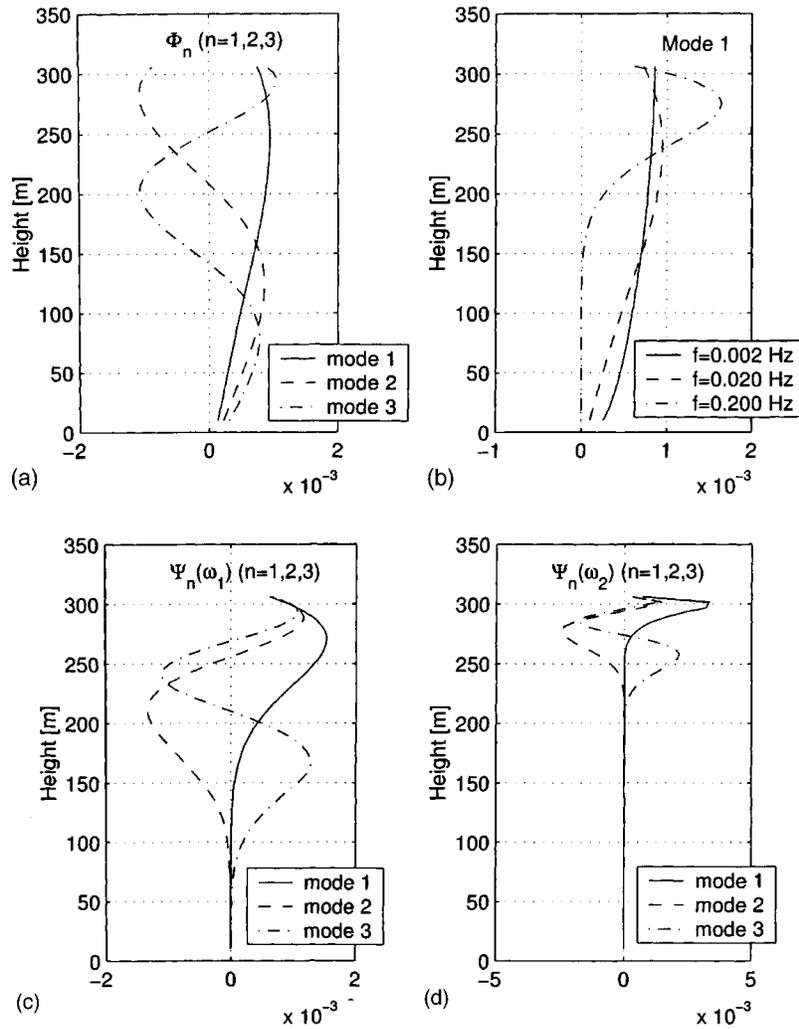
$$\mathbf{D} = [\mathbf{D}^{(1)}, \dots, \mathbf{D}^{(N_s)}]; \quad \mathbf{W} = [w_1, \dots, w_{N_s}]^T \quad (58)$$

In the case of wind velocity field, the XPSD matrix is often taken as real valued by neglecting the phase lag, which results in real-valued wind field eigenmodes. Furthermore, in certain cases, the eigenmodes change very slowly with respect to the frequency, and thus may be approximated as frequency independent by taking constant values at a fixed frequency, i.e., $\mathbf{\Psi}_n(\omega) = \mathbf{\Psi}_n(\omega_0)$ (Benfratello and Muscolino 1999; Kareem and Mei 2000). Consequently, the state-space model for $\mathbf{P}_n(t)$ can then be simplified by first establishing the state-space model for a scalar process $\lambda_n(t)$ with double-sided power spectrum $\Lambda_n(\omega)$ as

$$\mathbf{X}_0^{(n)}(k+1) = \mathbf{A}_0^{(n)}\mathbf{X}_0^{(n)}(k) + \mathbf{B}_0^{(n)}w_n(k) \quad (59)$$

$$\lambda_n(k) = \mathbf{C}_0^{(n)}\mathbf{X}_0^{(n)}(k) + D_0^{(n)}w_n(k) \quad (60)$$

and the state-space model for $\mathbf{P}_n(t)$ can be then derived with coefficient matrices as

$$\mathbf{A}^{(n)} = \mathbf{A}_0^{(n)}; \quad \mathbf{B}^{(n)} = \mathbf{B}_0^{(n)}; \quad \mathbf{C}^{(n)} = \mathbf{\Psi}(\omega_0)\mathbf{C}_0^{(n)}; \quad \mathbf{D}^{(n)} = \mathbf{\Psi}(\omega_0)\mathbf{D}_0^{(n)} \quad (61)$$

Example

The alongwind loading and associated response of a 76-story 306 m tall building with 76 DOFs is used for demonstrating the application of POD-based analysis schemes (Chen and Kareem 2000). The first and second natural frequencies of the building are 0.160 and 0.765 Hz, respectively. The modal damping ratio for each mode is assumed to be 0.01. The first two structural mode shapes are shown in Fig. 2. The mean wind velocity at the center of the ith story with height z_i above the ground is given by the power-law $U_i = U_{10}(z_i/10)^{0.33}$, where U_{10} is the mean wind velocity at 10 m above the ground and for example is taken as 15 m/s. The one-sided cross-spectrum of the alongwind fluctuations u_i and u_j ($i,j = 1, 2, \dots, 76$) is given by

$$S_{u_i u_j}(f) = \frac{4k_0 U_{10}^2}{f} \frac{X^2}{(1+X^2)^{4/3}} \exp\left(-\frac{k_z f|z_i - z_j|}{U_{10}}\right) \quad (62)$$

where $X = 1{,}200 f/U_{10}$, $k_0 = 0.03$ and $k_z = 7.7$.

The external loading vector is $\mathbf{P}(t) = \{P_1(t), P_2(t), \dots, P_{76}(t)\}^T$, where $P_i(t)$ is the alongwind fluctuating force at the ith story, which based on the quasi-steady and strip theories is modeled by

Table 1. Influence of Truncation of Higher Loading Modes on the Mean Square Loads and Their Effects (the Covariance Matrix-Based Proper Orthogonal Decomposition)

Mode number included	Ratio of the truncated value to the total value					
	P_1	P_{50}	P_{76}	F	$\hat{M}$	$\hat{Q}$
1-1	0.0835	0.5143	0.2761	0.9449	0.9872	0.9640
1-2	0.1753	0.5164	0.4196	0.9976	0.9984	0.9863
1-5	0.4797	0.7398	0.6070	0.9997	0.9997	0.9996
1-10	0.8529	0.8367	0.7153	0.9999	0.9999	0.9998
1-20	0.9778	0.9083	0.7922	0.9999	1.0000	0.9999
1-40	0.9964	0.9625	0.8226	0.9999	1.0000	1.0000
1-76	1.0000	1.0000	1.0000	1.0000	1.0000	1.0000
Total	$5.0826e+03$	$3.7635e+03$	$1.6400e+03$	$8.3046e+04$	$2.2006e+11$	$6.3354e+06$

$$P_i(t) = \rho A_i C_D U_i u_i(t) \qquad (63)$$

where ρ=air density; C_D=drag coefficient assumed to be 1.2; and A_i=tributary area for the ith story.

Proper Orthogonal Decomposition Representation of Wind Loads

Fig. 3(a) shows the eigenvalues of the covariance matrix of the loading vector $\mathbf{P}(t)$. The covariance matrix was calculated through the integration of the XPSD matrix over a frequency range from 0.002 Hz to 1 Hz with a frequency increment of 0.002 Hz. The first wind loading mode with dominant eigenvalue carries about 39% (i.e., $\Omega_1/\Sigma_{n=1}^{76}\Omega_n$) total energy of the loading process (i.e., $E[\mathbf{P}^T\mathbf{P}]=\Sigma_{n=1}^{76}\Omega_n$). A plot of the first three wind loading mode shapes is shown in Fig. 4(a) in terms of the distribution of load/unit area, i.e., $p_i(t)=P_i(t)/A_i$, which indicates almost sinusoidal variations. Figs. 3(b–d) show the eigenvalues of the XPSD matrix at varying frequencies, and at the first and second structural mode frequencies, respectively. It is noted that at the lower-frequency range the first eigenvalue is dominant, whereas at the higher-frequency range all the eigenvalues are of the same order, indicating that all the loading modes carry the same level of energy. The first wind loading mode carries about 11% total energy of the process at the first structural mode frequency, and about 3% at the second structural mode frequency. The first wind loading mode shapes at different frequencies, and the first three wind loading mode shape at first and second structural modal frequencies, are plotted in Figs. 4(b–d), which clearly reveal their frequency dependence.

In order to investigate the influence of higher-mode truncation on the global and local loads, the global wind loads, i.e., the generalized load in the first structural mode, F, base bending moment, $\hat{M}$, and base shear, $\hat{Q}$, and the local wind loads, i.e., the loads acting on the first, 50th and 76th stories, P_1, P_{50}, and P_{76}, are considered. The global wind loads are described by the integral of the wind load distribution weighted by the mode shape or global influence function. However, the local loads depend on the local wind load distribution at specific locations. Their mean square values (convariances) and PSDs are calculated based on the truncated process, which are then compared to those from the untruncated cases. The POD representations are based on both the covariance and XPSD matrices. The number of loading modes included are 1, 2, 5, 10, 20, 40, and 76.

Tables 1 and 2 present the mean square values of the local and global loads in terms of the ratios of these values to the original untruncated values. The first wind loading mode based on the covariance matrix carries about 8%, 51%, and 28% of the total energy of the local loading, P_1, P_{50}, and P_{76}, respectively. On the other hand, it carries about 95%, 99%, and 96% of the total energy of the global loads, F, $\hat{M}$, and $\hat{Q}$, respectively. A similar contribution of wind load modes based on the XPSD matrix is summarized in Table 2. The mean square pressure distributions along the building height corresponding to different loading modes included are plotted in Figs. 5(a and b). The exact pressure distribution contributed by all loading modes for this specific example is given by $(\rho C_D U_{10})^2(z_i/10)^{0.66}\sigma_{u_i}^2$, where $\sigma_{u_i}^2 = \int_0^\infty S_{u_iu_i}(f)df$. Figs. 6 and 7 show the influence of the truncating higher loading modes on the PSDs of P_{76} and F, and on the

Table 2. Influence of Truncation of Higher Loading Modes on the Mean Square Loads and Their Effects (the Cross Power Spectral Density Matrix-Based Proper Orthogonal Decomposition)

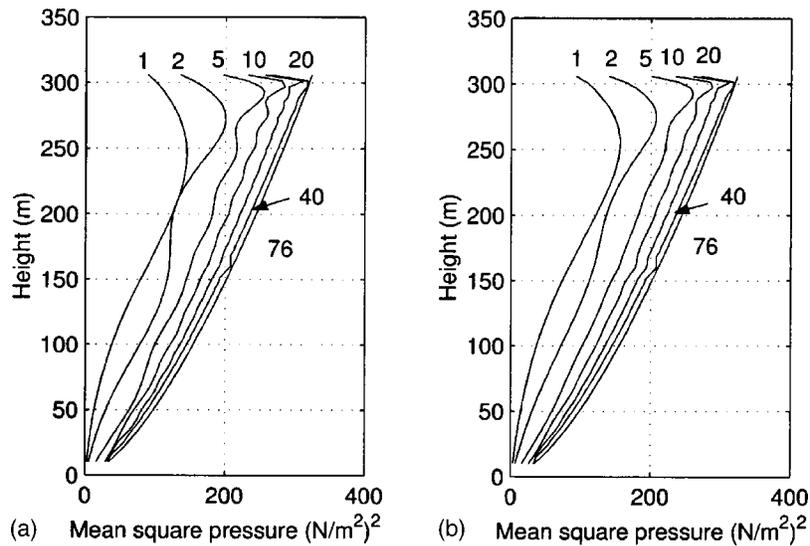| Mode number included	Ratio of the truncated value to the total value					
	P_1	P_{50}	P_{76}	F	$\hat{M}$	$\hat{Q}$
1-1	0.1031	0.5026	0.2840	0.9499	0.9761	0.9309
1-2	0.2087	0.5593	0.4303	0.9906	0.9883	0.9628
1-5	0.4719	0.7457	0.6180	0.9990	0.9985	0.9934
1-10	0.7630	0.8409	0.7259	0.9997	0.9996	0.9980
1-20	0.9855	0.9131	0.8016	0.9999	0.9999	0.9994
1-40	0.9976	0.9656	0.8386	0.9999	0.9999	0.9999
1-76	1.0000	1.0000	1.0000	1.0000	1.0000	1.0000
Total	$5.0826e+03$	$3.7635e+03$	$1.6400e+03$	$8.3046e+04$	$2.2006e+11$	$6.3354e+06$

Fig. 5. Influence of truncating higher wind loading modes on the mean square pressures: (a) Based on the covariance matrix; and (b) based on the cross power spectral density matrix

XPSDs between P_1 and P_{76} and between P_{50} and P_{76}. A sample of simulated time histories of P_{76} and F, consisting of contributions of all loading modes and only each of the lower five loading modes, is shown in Fig. 8. The spectral representation approach was employed for this simulation. Results clearly demonstrate that the truncation of higher modes results in a significant reduction in the local wind loads, particularly, at the higher-frequency range, whereas only a small number of loading modes can approximate the global wind loads with reasonable accuracy. The

contribution of higher loading modes to the global wind loading is insignificant due to their spatial variations with higher wave numbers.

Based on the frequency dependent eigenvalues of XPSD matrix, it is noted that in the low-frequency range, inclusion of only a small number of predominant lower modes can achieve accurate description of the original process; however, at a high-frequency range, higher modes are required to accurately describe the process. This tends to defeat the purpose of the reduced-order
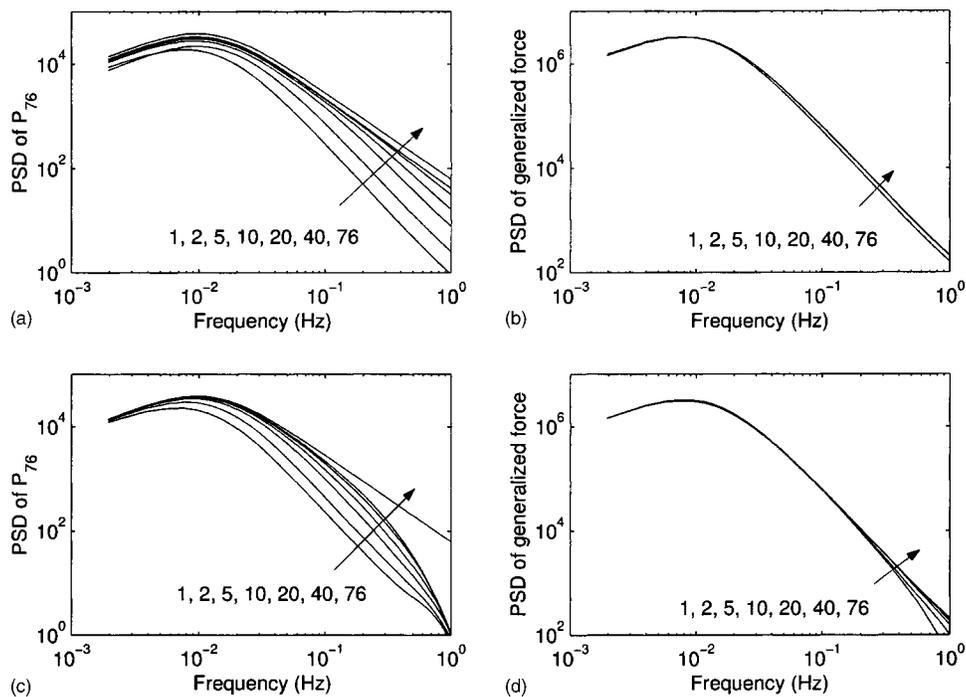

Fig. 6. Influence of truncating higher wind loading modes on the power spectral densities of local and global loads: (a) Based on the covariance matrix (local load P_{76}); (b) based on the covariance matrix (global load F); (c) based on the cross power spectral density (XPSD) matrix (local load P_{76}); and (d) based on the XPSD matrix (XPSD between P_{50} and P_{76})
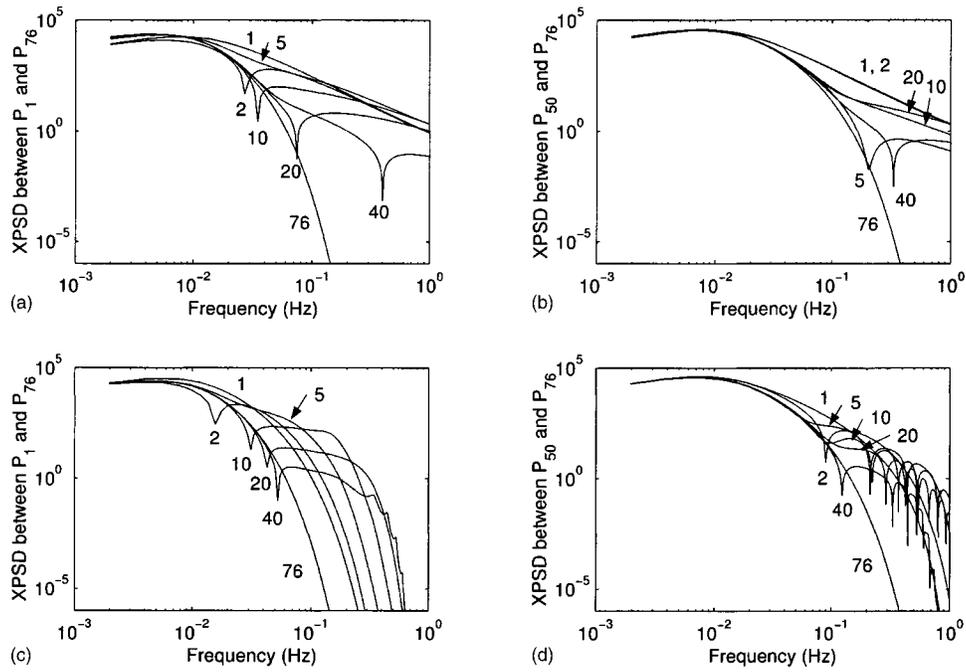
Fig. 7. Influence of truncating higher wind loading modes on the cross power spectral density (XPSDs) between P_1 and P_{76} and between P_{50} and P_{76}: (a) Based on the covariance matrix (XPSD between P_1 and P_{76}); (b) based on the covariance matrix (XPSD between P_{50} and P_{76}); (c) based on the XPSD matrix (XPSD between P_1 and P_{76}); and (d) based on the XPSD matrix (XPSD between P_{50} and P_{76})
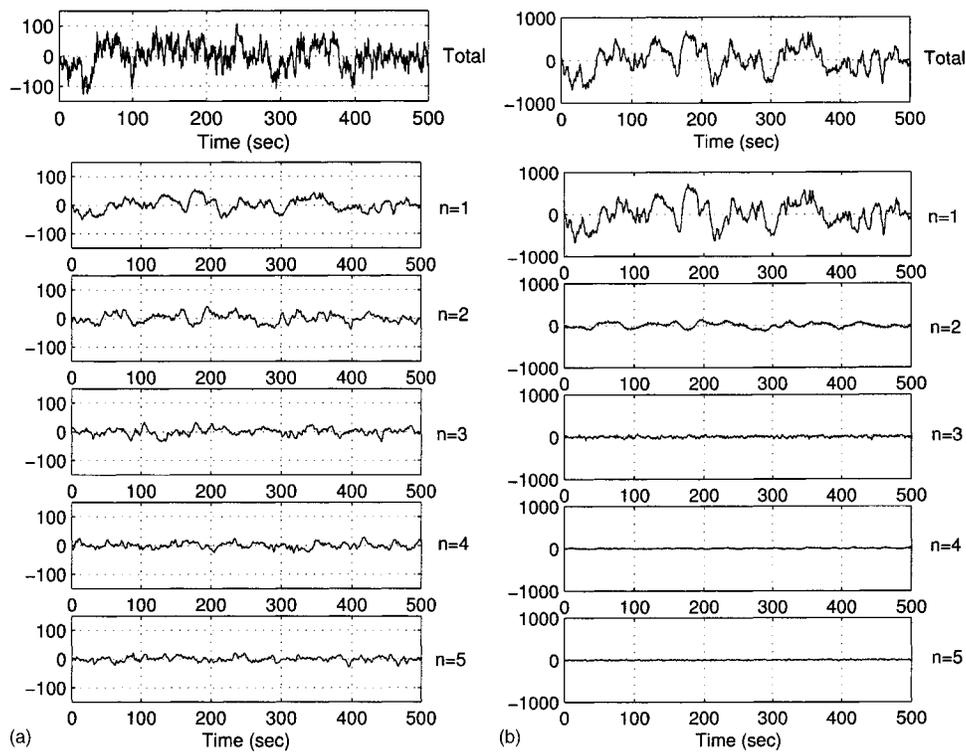

Fig. 8. Time history simulations of the local and global loads in terms of components associated with each of lower five loading modes: (a) Local load, P_{76}; and (b) generalized modal force in first mode, F

Table 3. Mean Square Background Response in Terms of the Contribution of Each Wind Loading Mode

Mode number	Ω_n ($\times 10^4$)	$\sigma^2_{Y_b}$ ($\times 10^{-4}$) (m^2)	$\sigma^2_{M_b}$ ($\times 10^{11}$) [(N m)^2]	$\sigma^2_{Q_b}$ ($\times 10^6$) (N^2)
1	9.2835	9.8340	2.1724	6.1072
2	3.4946	0.6764	0.0248	0.1414
3	1.9977	0.0141	0.0015	0.0663
4	1.3240	0.0162	0.0013	0.0120
5	0.9546	0.0010	0.0000	0.0059
$\Sigma^{76}_{n=1}$	23.8299	10.5457	2.2006	6.3354

representation using the POD technique. The fluctuating wind velocities and wind loads become statistically less coherent at the higher-frequency range. In general, a random field with weak coherence requires a relatively large number of modes in the reconstruction of original field. Therefore, the POD representation is numerically advantageous particularly for well-correlated random fields, such as the pressure fields on low-rise buildings and roofs and side faces of tall buildings. Its effectiveness in modeling poorly correlated random field is rather limited, particularly, for representing high-frequency fluctuations that correspond to the small size of turbulence.

Contribution of Wind Loading Modes to Response

Table 3 presents the contributions of wind loading modes based on the covariance matrix to the background response components, i.e., the displacement at the building top, Y_b, base bending moment response, M_b, and base shear response, Q_b. The first wind loading mode containing only 39% total energy of the loading process contributed about 93, 99, and 96% (i.e., $c_1^2 \Omega_1 / \Sigma^{76}_{n=1} c_n^2 \Omega_n$) to the mean square displacement, base moment, and base shear, respectively. The large contribution of the first wind loading mode is not only attributed to its large eigenvalue, but also due to its larger contribution coefficient c_1, which is the projection of the wind loading mode shape on the influence function. A lower value of this coefficient implies approximate orthogonality between these spatial functions. From the wind loading mode shapes and the influence functions of responses, it can be readily ascertained

that the higher modes with higher wave numbers in space contribute less to the global response. The structure in the loading response chain participates as a low-pass filter such that the global response results only from the external load with lower wave numbers in space. For local response components, the relative contribution of the first loading mode decreases, and consequently additional loading modes are required for accurate response estimation.

Table 4 shows the contribution of wind loading modes based on the XPSD matrix to the resonant response in the first and second structural modes, i.e., displacement at the top, Y_{jr}, base bending moment, M_{jr}, and base shear, Q_{jr} ($j=1,2$). As mentioned previously, the contribution of each wind loading mode depends on the eigenvalue and the projection of wind loading mode shape on the structural mode shape. The loading modes which depend on the spatial variation of the fluctuating wind pressure field do not necessarily ensure orthogonality to the structural modes characterized by the mass and stiffness distributions of the structure. In this specific example, the mean square resonant response is dominated by the response in the first structural mode (more than 97%), which is contributed mainly by the first loading mode (about 91%). However, not only the first wind loading mode, but the second and tenth wind loading modes also have notable contributions of about 11% to the response in the second mode. The ratios between the mean square background and resonant response components, i.e., tip displacement, base moment, and base shear, are 0.33, 0.36, and 0.47, respectively.

Table 4. Mean Square Resonant Modal Response in Terms of the Contribution of each Wind Loading Mode

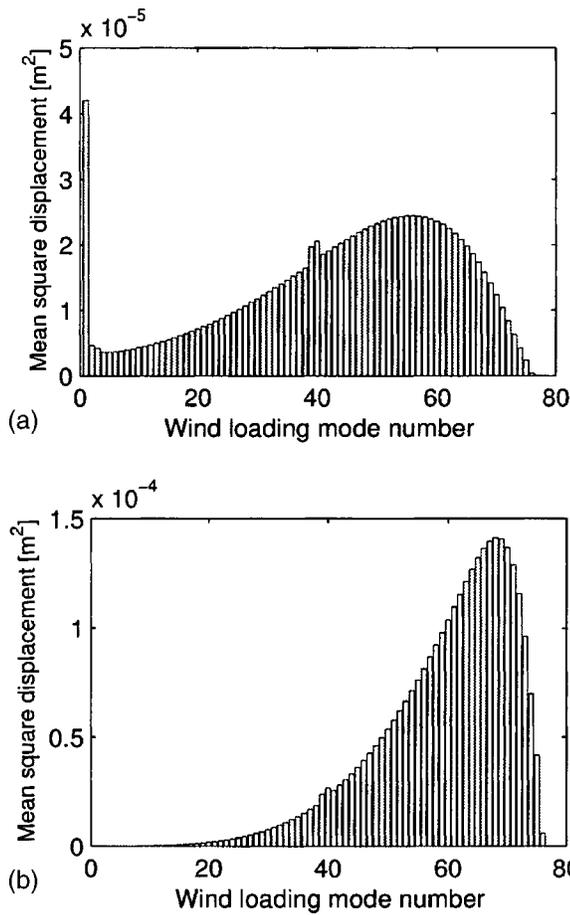| Mode number	$\Lambda_n(f_j)$ ($\times 10^4$)	$\chi^2_{jn}(f_j)$	$\sigma^2_{Y_{jr}}$ ($\times 10^{-4}$) (m^2)	$\sigma^2_{M_{jr}}$ ($\times 10^{11}$) [(N m)^2]	$\sigma^2_{Q_{jr}}$ ($\times 10^6$) (N^2)
First structural modal response					
1	2.0777	0.8380	44.2790	8.6465	19.0130
2	1.7423	0.0323	1.3994	0.2733	0.6009
3	1.5021	0.0816	3.0009	0.5860	1.2886
4	1.2865	0.0001	0.0030	0.0006	0.0013
5	1.1086	0.0167	0.4451	0.0869	0.1911
$\Sigma^{76}_{n=1}$	19.2264		49.3416	9.6351	21.1869
Second structural modal response					
1	0.0457	0.2691	0.0028	0.0109	0.2158
2	0.0415	0.0851	0.0008	0.0031	0.0614
3	0.0395	0.0025	0.0000	0.0001	0.0017
4	0.0378	0.0009	0.0000	0.0000	0.0006
5	0.0364	0.0068	0.0001	0.0002	0.0042
$\Sigma^{76}_{n=1}$	1.4230		0.0071	0.0278	0.5506

Fig. 9. Contribution of each wind loading mode to the mean square displacement at the building top (based on the Cholesky decomposition): (a) Background component; and (b) resonant component

For the sake of comparison, the response analysis based on the Cholesky decomposition of the loading process is also carried out by using $\mathbf{R_P} = \mathbf{L}_R \mathbf{L}_R^T$ and $\mathbf{S_P}(\omega) = \mathbf{L}_S(\omega) \mathbf{L}_S^*(\omega)$, where $\mathbf{L}_R$ and $\mathbf{L}_S(\omega)$ are the lower/upper triangular matrices. Similar formulations linking the background response and $\mathbf{L}_R$, and the resonant response and $\mathbf{L}_S(\omega)$, can be obtained by replacing $\mathbf{\Phi}\sqrt{\mathbf{\Omega}}$ with $\mathbf{L}_R$, and replacing $\mathbf{\Psi}(\omega)\sqrt{\mathbf{\Lambda}(\omega)}$ with $\mathbf{L}_S(\omega)$.
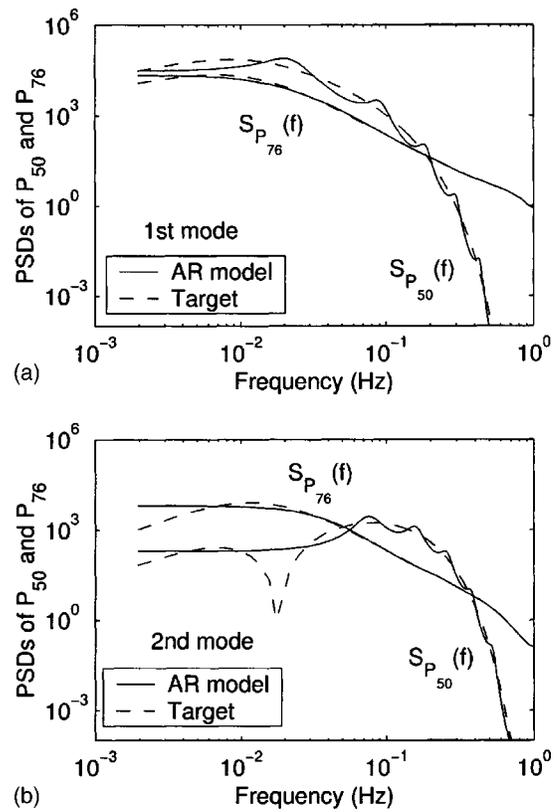

Fig. 10. Comparison of PSDs for P_{50} and P_{76} based on the autoregressive models: (a) First loading mode; and (b) second loading mode

Figs. 9(a and b) describe the contribution of each wind loading mode, based on the Cholesky decomposition, to the background and resonant (first structural modal response) components of the displacement at the top of the building. Obviously, the Cholesky decomposition requires many more loading modes for an accurate representation of the covariance and spectral matrices, and the attendant background and resonant responses. The POD, which is based on Schur decomposition, permits truncation of higher modes and it is the optimal orthogonal basis function for reduced-order modeling of large-size random fields.
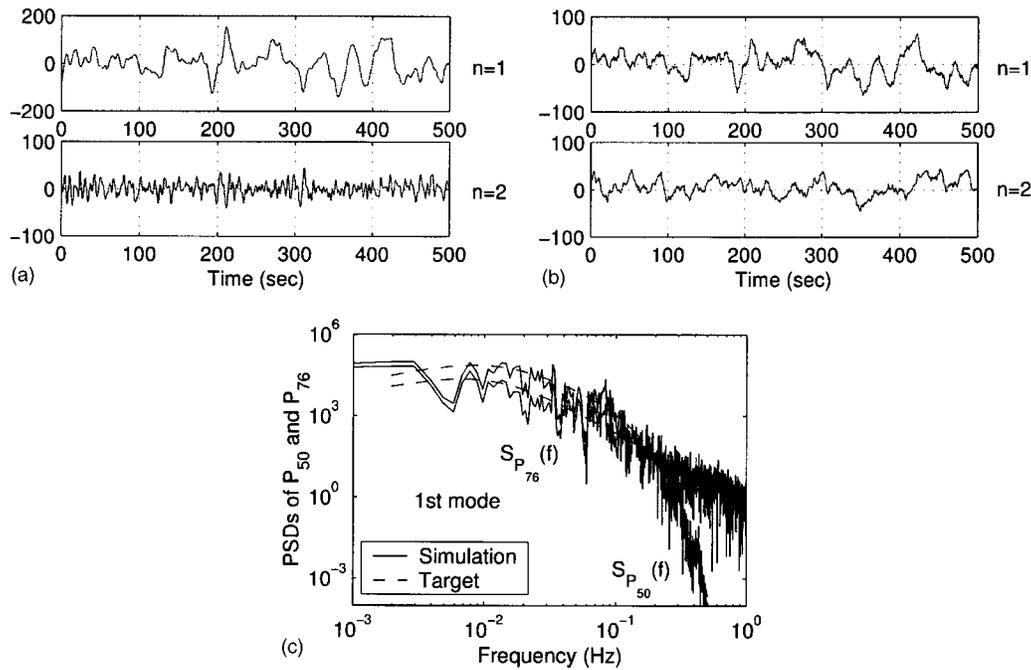
Table 5. Coefficients of Autoregressive Models for P_{50} and P_{76}

$\sigma_{lj}^{(n)}$	First loading mode ($n=1$)		Second loading mode ($n=2$)	
	P_{50} ($j=50$)	P_{76} ($j=76$)	P_{50} ($j=50$)	P_{76} ($j=76$)
1	6.8508	1.3401	5.2783	1.8137
2	−22.4968	−0.4259	−14.1361	−1.2941
3	46.9683	0.2166	25.3332	0.7546
4	−69.3838	−0.1838	−33.7738	−0.4187
5	76.0056	0.0886	35.0880	0.2017
6	−62.6049	−0.0692	−28.8214	−0.1089
7	38.2751	0.0433	18.4921	0.0585
8	−16.5912	−0.0346	−8.8708	−0.0397
9	4.5880	−0.0232	2.8709	0.0247
10	−0.6113	−0.0195	−0.4780	−0.0174
$\sigma_j^{(n)}$	0.0256	3.1963	0.2456	2.0703

Fig. 11. Sample of simulated time histories of P_{50} and P_{76}: (a) Simulated time histories of P_{50}; (b) simulated time histories of P_{76}; and (c) comparison of power spectral densities

State-Space Modeling of Wind Loads

Utilizing the XPSD matrix-based POD technique, the state-space modeling of the multicorrelated loading process can be realized by the state-space modeling of each subprocess associated with each loading mode independently. Table 5 summarizes the coefficients of the AR models with an order of 10 for wind loads P_{50} and P_{76} associated with first and second loading modes. The time interval was chosen as 0.5 s. Figs. 10(a and b) compare the PSDs based on the AR models with the target functions. A sample of simulated time histories based on the first and second loading modes, respectively, are plotted in Fig. 11(a). The PSDs calculated from the time histories are compared to the target functions in Fig. 11(b). Results shown Figs. 10 and 11 demonstrate the effectiveness and accuracy of the AR model and simulation in describing the loading process.

It is noted that the size of state-space representation of the process depends on the order of the AR model. This order may be reduced if the ARMA model is employed, as a process may be described by an ARMA model with a lower order than the AR model, however, evaluation of the ARMA model requires a more sophisticated algorithm. It is also worth mentioning that direct application of a multivariate the AR or ARMA model scheme can further aid in reducing the size of the state-space representation (Chen and Kareem 2001). However, the POD technique-based framework provides not only a physically more meaningful representation, but it is also computationally more straightforward.

Concluding Remarks

The transformation of correlated vector-valued loading process to uncorrelated or noncoherent subprocesses through the POD technique, based on both the covariance or XPSD matrices, facilitates data compression and reduced-order modeling of a large-size random loading field. This is achieved by truncating higher modes of the random field without any significant loss of accuracy, which is akin to the modal analysis in structural dynamics. In addition to the physical insight gained from the loading modes based on their spatial variations, the uncorrelated or noncoherent feature of the reduced-order loading representation aids in expediting the response analysis. This is particularly significant for the prediction of correlated structural response components of large number of DOF structures. Furthermore, the POD of the loading process renders a physically meaningful linkage between the wind loading and the attendant background and resonant responses of structures.

An example of a tall building aided in demonstrating that the truncation of higher wind loading modes results in a notable loss of information, particularly, at the higher-frequency range where wind loads have a weak correlation. Since the local loads and their effects are very sensitive to the higher wind loading modes, a truncation of higher loading modes can notably affect the accurate representation of these loads and their effects. In contrast, the higher wind loading modes have an insignificant contribution to the global loads and their effects due to lower values of eigenvalues (low energy) associated with these and, more importantly, due to the nature of their spatial variation. In general, consideration of only a small number of modes can adequately represent a well-correlated random loading field, conversely, a weakly correlated loading field requires inclusion of a large number of modes, which may compromise the attractiveness of the computational features of the POD technique.

The POD technique based on the XPSD matrix facilitates the simulation and state-space modeling of a correlated vector-valued random process. The state-space modeling of a large-size wind field based on the factorization of the XPSD matrix and subsequent realization of the transfer function matrix has been noted to be a challenging task. The POD-based technique presents an efficient tool for the state-space modeling of such processes/fields. A numerical example using the spatiotemporarily varying dy-

namic wind loading field on the example building demonstrated the effectiveness and accuracy of the POD-based framework.

Acknowledgment

References

Armitt, J. (1968). "Eigenvector analysis of pressure fluctuations on the west instrumented cooling tower." *Internal Rep. RD/L/N114/68*, Central Electricity Research Laboratories, U.K.

Benfratello, S., and Muscolino, G. (1999). "Filter approach to the stochastic analysis of MDOF wind-excited structures." *Probab. Eng. Mech.*, 14, 311–321.

Bienkiewicz, B., Tamura, Y., Hann, H. J., Ueda, H., and Hibi, K. (1995). "Proper orthogonal decomposition and reconstruction of multichannel roof pressure." *J. Wind. Eng. Ind. Aerodyn.*, 54–55, 369–381.

Cao, Y., Xiang, H., and Zhou, Y. (2000). "Simulation of stochastic wind velocity field on long-span bridges." *J. Eng. Mech.*, 126(1), 1–6.

Carassale, L., Piccardo, G., and Solari, G. (2001). "Double-model transformation and wind engineering applications." *J. Eng. Mech.*, 127(5), 432–439.

Carassale, L., and Solari, G. (2002). "Wind modes for structural dynamics: A continuous approach." *Probab. Eng. Mech.*, 17, 157–166.

Chen, X., and Kareem, A. (2000). "On the application of stochastic decomposition in the analysis of wind effects." *Proc., Int. Conf. on Advances in Struct. Dyn. (ASD 2000)*, The Hong Kong Polytechnic University, Hong Kong, 135–142.

Chen, X., and Kareem, A. (2001). "Aeroelastic analysis of bridges under multicorrelated winds: Integrated state-space approach." *J. Eng. Mech.*, 127(11), 1124–1134.

Davenport, A. G. (1995). "How can we simplify and generalize wind loads?" *J. Wind. Eng. Ind. Aerodyn.*, 54–55, 657–669.

Di Paolo, M., and Gullo, I. (2001). "Digital generation of multivariate wind field processes." *Probab. Eng. Mech.*, 16, 1–10.

Ghanem, R., and Spanos, P. (1991). *Stochastic finite elements: A spectral approach*, Springer, Berlin.

Goßmann, E., and Walter, H. B. (1983). "Analysis of multicorrelated wind-excited vibrations of structures using the covariance method." *Eng. Struct.*, 5, 264–272.

Holmes, J. D. (1992). "Optimized peak load distributions." *J. Wind. Eng. Ind. Aerodyn.*, 41–44, 267–276.

Holmes, J. D., Sankaran, R., Kwok, K. C. S., and Syme, M. J. (1997). "Eigenvector modes of fluctuating pressures on low-rise building models." *J. Wind. Eng. Ind. Aerodyn.*, 69–71, 697–707.

Kareem, A. (1978). "Wind excited motion of buildings." PhD dissertation, Dept. of Civil Engineering, Colorado State Univ., Fort Collins, Colo.

Kareem, A. (1997). "Modeling of base-isolated buildings with passive dampers under winds." *J. Wind. Eng. Ind. Aerodyn.*, 72, 323–333.

Kareem, A. (1999). "Analysis and modeling of wind effects: Numerical techniques." *Wind Engineering into the 21st Century*, A. Larsen, G. L. Larose, and F. M. Livesy, eds., Balkema, Rotterdam, The Netherlands, 43–54.

Kareem, A., and Cermak, J. E. (1984). "Pressure fluctuations on a square building model in boundary-layer flows." *J. Wind. Eng. Ind. Aerodyn.*, 16, 17–41.

Kareem, A., and Mei, G. (2000). "Stochastic decomposition for simula-

tion and modal space reduction in wind induced dynamics of structures." *Applications of statistics and probability*, R. E. Melchers and M. G. Stewart, eds., Balkema, Rotterdam, 757–764.

Lee, B. E. (1975). "The effect of turbulence on the surface pressure field of a square prism." *J. Fluid Mech.*, 69, 263–282.

Li, Y., and Kareem, A. (1989). "On stochastic decomposition and its application in probabilistic dynamics." *Proc., 5th Int. Conf., on Structural Safety and Reliability (ICOSSAR'89)*, A. H.-S. Ang, M. Shinozuka, and G. I. Schueller, eds., ASCE, New York.

Li, Y., and Kareem, A. (1990). "ARMA system in wind engineering." *Probab. Eng. Mech.*, 5(2), 50–59.

Li, Y., and Kareem, A. (1991). "Simulation of multivariate nonstationary random processes by FFT." *J. Eng. Mech.*, 117(5), 1037–1058.

Li, Y., and Kareem, A. (1993). "Simulation of multivariate random processes: Hybrid DFT and digital filtering approach." *J. Eng. Mech.*, 119(5), 1078–1098.

Li, Y., and Kareem, A. (1995). "Stochastic decomposition and application to probabilistic dynamics." *J. Eng. Mech.*, 121(1), 162–174.

Li, Y., and Kareem, A. (1997). "Simulation of multivariate nonstationary random processes: Hybrid DFT and digital filting approach." *J. Eng. Mech.*, 123(12), 1302–1310.

Lin, J. H., Zhang, W. S., and Li, J. J. (1994). "Structural responses to arbitrarily coherent stationary random excitations." *Comput. Struct.*, 50(5), 629–633.

Loeve, M. (1963). *Probability theory*, Van Nostrand, Princeton, N.J.

Lumley, J. L. (1970). *Stochastic tools in turbulence*, Academic, San Diego.

Maan, J. (1998). "Wind field simulation." *Probab. Eng. Mech.*, 13(4), 269–282.

Matsumoto, Y., Fujino, Y., and Kimura, K. (1996). "Wind-induced gust response analysis based on state space formulation." *J. Struct. Mech. Earthquake Eng.*, 543/I-36, 175–186 (in Japanese).

Ogata, K. (1994). *Discrete-time control systems*, Prentice–Hall, Englewood Cliffs, N.J.

Rocha, M. M., Cabral, S. V. S., and Riera, J. D. (2000). "A comparison of proper orthogonal decomposition and Monte Carlo simulation of wind pressure data." *J. Wind. Eng. Ind. Aerodyn.*, 84, 329–344.

Shinozuka, M., and Jan, C. M. (1972). "Digital simulation of random processes and its applications." *J. Sound Vib.*, 25(10), 111–128.

Shinozuka, M., Yun, C.-B., and Seya, H. (1990). "Stochastic methods in wind engineering." *J. Wind. Eng. Ind. Aerodyn.*, 36, 829–843.

Shinozuka, M., and Deodatis, G. (1996). "Simulation of multidimensional Gaussian stochastic fields by spectral representation." *Appl. Mech. Rev.*, 49(1), 29–53.

Spanos, P. D., and Zeldin, B. A. (1998). "Monte Carlo treatment of random fields: A broad perspective." *Appl. Mech. Rev.*, 51(3), 219–237.

Suhardjo, J., Spencer, B. F., Jr., and Kareem, A. (1992). "Active control of wind excited buildings: A frequency domain based design approach." *J. Wind. Eng. Ind. Aerodyn.*, 43(1–3), 1985–1996.

Tamura, Y., Suganuma, S., Kikuchi, H., and Hibi, K. (1999). "Proper orthogonal decomposition of random wind pressure field." *J. Fluids Struct.*, 13, 1069–1095.

Therrien, C. W. (1992). *Discrete random signals and statistical signal processing*, Prentice–Hall, Englewood Cliffs, N.J.

van Trees, H. I. (1968). *Detection, estimation, and modulation theory. Part 1*, Vol. 1, Wiley. New York.

Vasta, M., and Schueller, G. I. (2000). "Phase space reduction in stochastic dynamics." *J. Eng. Mech.*, 126(6), 626–632.

Xu, Y. L., Zhang, W. S., Ko, J. M., and Lin, J. H. (1999). "Pseudoexcitation method for vibration analysis of wind-excited structures." *J. Wind. Eng. Ind. Aerodyn.*, 83, 443–454.

Yamazaki, F., and Shinozuka, M. (1990). "Simulation of stochastic fields by statistical preconditioning." *J. Eng. Mech.*, 116(2), 268–287.